1998-09

Optimization of the Strength-Fracture Toughness Relation in Particulate-Reinforced Aluminum Composites via Control of the Matrix Microstructure

Dutta, I.; Quiles, F.N.; McNelley, T.R.; Nagarajan, R.

Optimization of the Strength-Fracture Toughness Relation in Particulate-Reinforced Aluminum Composites via Control of the Matrix Microstructure

I. DUTTA, F.N. QUILES, T.R. McNELLEY, and R. NAGARAJAN

The evolution of the microstructure and mechanical properties of a 17.5 vol. pct SiC particulate–reinforced aluminum alloy 6092–matrix composite has been studied as a function of postfabrication processing and heat treatment. It is demonstrated that, by the control of particulate distribution, matrix grain, and substructure and of the matrix precipitate state, the strength-toughness combination in the composite can be optimized over a wide range of properties, without resorting to unstable, underaged (UA) matrix microstructures, which are usually deemed necessary to produce a higher fracture toughness than that displayed in the peak-aged condition. Further, it is demonstrated that, following an appropriate combination of thermomechanical processing and unconventional heat treatment, the composite may possess better stiffness, strength, *and* fracture toughness than a similar unreinforced alloy. In the high- and low-strength matrix microstructural conditions, the matrix grain and substructure were found to play a substantial role in determining fracture properties. However, in the intermediate-strength regime, properties appeared to be optimizable by the utilization of heat treatments only. These observations are rationalized on the basis of current understanding of the grain size dependence of fracture toughness and the detailed microstructural features resulting from thermomechanical treatments.

I. INTRODUCTION

DISCONTINUOUSLY reinforced aluminum (DRA) composites are promising candidates for a number of aerospace and automotive applications, because they display significantly higher stiffness-to-weight and strength-to-weight ratios and possess better wear resistance and elevated-temperature properties than unreinforced aluminum alloys. However, DRA composites typically have a low fracture toughness relative to unreinforced aluminum. It has recently become quite apparent that, unless the intrinsic fracture toughness of DRA can be systematically and predictably improved, its acceptance as a reliable structural material will not be forthcoming.

Several detailed studies and reviews of the fracture behavior of DRA have been published during the last decade.[1–12] A number of different microstructural variables, including the volume fraction,[4,9,16] size,[4] shape,[14,15,16] and spatial distribution of the reinforcement phase,[2,9,13,18] as well as the details of the matrix microstructure[2,9,17–20] and interface composition,[2,21] have been shown to play important roles in determining the deformation and fracture behavior of DRA.

Two different fracture mechanisms have been commonly observed in DRA in the absence of interfacial damage (*e.g.*, References 9 and 19). In composites with matrices having high strength and a relatively low work hardening rate (*e.g.*, in the artificially peak-aged condition), fracture is typically dominated by the crack nucleation event, which occurs by particle cracking accompanied by a high degree of strain localization. In this case, particle cracking is rapidly followed by final fracture. On the other hand, in composites with relatively soft matrices and a high work hardening rate (*e.g.*, in the naturally aged condition), the extent of strain localization is limited, and significant tensile ductility may be obtained following the initial particle fracture events.[9,19] In general, damage initiation is most likely to begin either by cracking of the larger particles[2,4,9,19,22] or by matrix microvoid nucleation and growth within clusters of small particles.[9,11] Preferential cracking of the larger particles is thought to be associated with the increased flaw density in large particles in conjunction with the increased local stress supported by large particles,[2,4,9,19] whereas matrix cracking within clusters is attributable to the presence of large hydrostatic tension between clustered particles.[9,11] Additionally, damage may initiate by facile nucleation of microvoids at incoherent precipitates at particle-matrix interfaces, as observed in a Al-Zn-Mg-matrix DRA with an overaged (OA) matrix.[2] Indeed, comparison of the fracture behavior of DRA with underaged (UA) and OA matrices in identical hardness states has shown that both crack initiation and propagation fracture toughnesses are greater in the UA matrix, with the fracture process being dominated by particle fracture in the UA state and by near-interface fracture in the OA state.[6]

It is clear from the previous paragraphs that, for a given particulate volume fraction and shape, the two parameters which have the greatest influence on both the micromechanisms of, and the resistance to, fracture in DRA are (1) the particulate spatial distribution and (2) the matrix microstructural condition. It is generally appreciated that increased uniformity in particulate spatial distribution is beneficial to the overall fracture properties, and that this

I. DUTTA, Associate Professor of Materials Science, T.R. McNELLEY, Professor of Materials Science, and R. NAGARAJAN, NRC Postdoctoral Research Associate, are with the Department of Mechanical Engineering, Naval Postgraduate School, Monterey, CA 93943. F.N. QUILES, formerly Graduate Student, Department of Mechanical Engineering, Naval Postgraduate School, is with the United States Navy.

Manuscript submitted June 19, 1997.

Table I. Nominal Composition of Aluminum Alloy 6092

Element	Weight Percent
Silicon	0.40 to 0.80
Magnesium	0.80 to 1.20
Copper	0.70 to 1.00
Manganese	0.15 max.
Chromium	0.15 max.
Zinc	0.25 max.
Titanium	0.15 max.
Iron	0.70 max.
Oxygen	0.05 to 0.50
Others, each	0.05 max.
Others, total	0.15 max.
Aluminum	remainder

Table II. Sample Nomenclature and Processing Conditions

Nomenclature	Total True Strain	Strain Rate (s^{-1})	Extrusion Temperature (°C)
PSN	5.67	5.6	400
Non-PSN	5.67	0.6	400
Intermediate	5.67	5.6	450

may be achieved *via* appropriate postfabrication deformation processes (*e.g.*, References 13, 18, and 21). However, previous work has shown that the true strains required to eliminate the obvious microstructural artifacts of inhomogeneity in particle distribution, such as clustering/banding of particles (which are highly detrimental to the fracture properties, as mentioned previously) are usually very large (~4 to 5).[23] This poses a practical limit to the extent of property improvement achievable *via* particle redistribution alone, necessitating the development of systematic approaches to exploit the matrix in order to optimize properties. Precise and innovative control of matrix microstructure in the quest for higher fracture toughness in DRA materials is particularly important, since it is clear from published data (*e.g.*, References 2 and 7) that conventional aging treatments are unable to produce toughness levels superior to those obtained in the -T6 condition while producing a stable microstructure (although underaging enhances toughness at the expense of strength, it does so by producing an unstable microstructure which naturally age-hardens during service). Therefore, it appears that only by clever design of (1) the matrix microstructure (including grain, subgrain, and dislocation structures) and (2) the precipitate state, *via* a combination of post-fabrication processing and unconventional heat treatments, may one be able to further optimize the strength-toughness relation in DRA. However, the role of matrix microstructure, particularly with regard to the grain/substructure and unconventional precipitate states, on the overall fracture behavior of DRA is unclear at present.

Although it is well known that the microstructural scale can have a significant impact on the fracture behavior of metallic alloys (*e.g.*, References 24 through 28), refinement of the matrix grain/substructure as a mechanism for improving the fracture toughness of DRA had not been investigated systematically until recently.[20] In that study,[20] the mechanism of particle-stimulated nucleation (PSN) of recrystallization was utilized to refine the matrix grain structure *via* deformation processing, and it was demonstrated that significant improvements in the fracture toughness of DRA may be obtained *via* control of the matrix microstructure. The phenomeon of PSN of recrystallization during thermomechanical processing (TMP) of particle-containing Al alloys was first reported by Humphreys[29] and has since been verified to occur during TMP of DRA.[18,30–32] If the temperature is low enough to minimize recovery effects during TMP, then the straining will result in the development of local lattice rotations within the deformation zones surrounding large reinforcement particles.[29–31,33,34] Stable recrystallization nuclei may then form within such deformation zones and grow if sufficient strain energy has been imparted by processing. For a given strain, strain rate, and temperature, deformation zones increase in size as particle size increases and, therefore, larger particles are more efficient at stimulating nucleation, although the resulting grain size may be larger.[29] Particle-stimulated nucleation of recystallization has been successfully utilized to refine matrix grain structures in a number of DRA composites,[18,20,30–32] although the impact of such refinement on fracture toughness has not been studied in detail.

This article presents the results of experiments designed to tailor the strength-fracture toughness relationship in DRA by postfabrication TMP. Particular emphasis has been placed on ascertaining the roles of (1) matrix microstructure, including grain and subgrain structures, and (2) precipitate states, produced by unconventional heat treatments, on the observed properties and the mechanisms of damage initiation and propagation.

II. EXPERIMENTAL

The material used in the present experiments was a powder metallurgically (P/M) processed aluminum alloy 6092, reinforced with 17.5 vol. pct SiC particulates with a mean particle size of 7 μm, fabricated by DWA Composites (Chatsworth, CA). The nominal elemental composition of the 6092 Al alloy is given in Table I.[35] The as-consolidated composite billet, which had a diameter of 0.4826 m, was subsequently extruded to a true strain of 3.38 at 500 °C, producing a billet of 0.0889 m in diameter. Following this initial extrusion, the billet was trimmed to a diameter of 0.0762 m and then extruded through streamlined dies under three different conditions to produce billets with rectangular cross sections of 0.0377 × 0.0123 m, yielding an additional true strain of 2.29 (total true strain of 5.67 following powder consolidation). The three processing conditions were carefully selected based on the theory of PSN,[29,32] such that one corresponded to a regime where PSN is likely to occur (strain rate $\dot{\varepsilon}$ = 5.6/s, T = 400 °C), the second corresponded to a regime where PSN is not expected (strain rate $\dot{\varepsilon}$ = 0.6/s, T = 400 °C), and the third represented conditions intermediate between the PSN and nonPSN states (strain rate $\dot{\varepsilon}$ = 5.6/s, T = 450 °C). The processing conditions for the three states are listed in Table II and have been designated as the PSN, nonPSN, and intermediate states, respectively. These conditions were arrived at by determining the critical strain rate ($\dot{\varepsilon}_{cr}$) necessary to result in PSN at the given temperature, for the given alloy and particle size, based on the approach of Reference 30, and ensuring that $\dot{\varepsilon} > \dot{\varepsilon}_{cr}$ for the PSN case, $\dot{\varepsilon} < \dot{\varepsilon}_{cr}$ for the nonPSN case, and $\dot{\varepsilon} \sim \dot{\varepsilon}_{cr}$ for the intermediate case.

Table III. Heat-Treatment Designations and Conditions

Designation	Solution Treatment	Heat-Treatment Conditions
-T6	560 °C, 1.5 h	170 °C, 8 h
-T4	560 °C, 1.5 h	natural aging, 9 months
-450	450 °C, 20 min	none
-450-170	450 °C, 20 min	170 °C, 8 h
-480-170	480 °C, 20 min	170 °C, 8 h
-560-450	560 °C, 1.5 h	450 °C, 20 min
-560-450-170	560 °C, 1.5 h	step 1: 450 °C, 20 min, water quench step 2: 170 °C, 8h

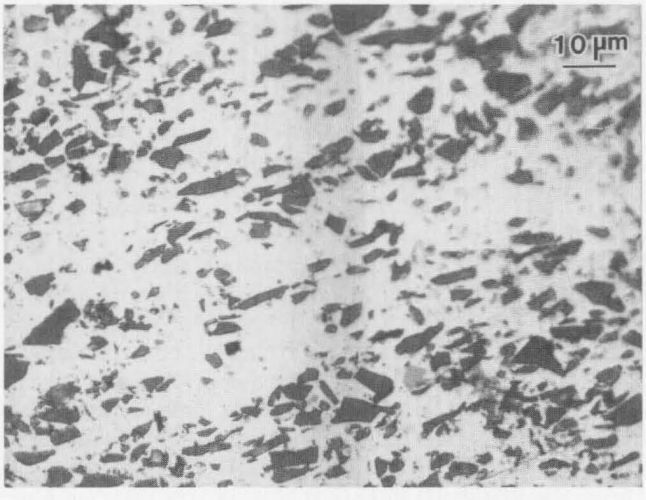

Fig. 1—Distribution of SiC_p in the experimental composite after initial extrusion to a true strain of 3.38.

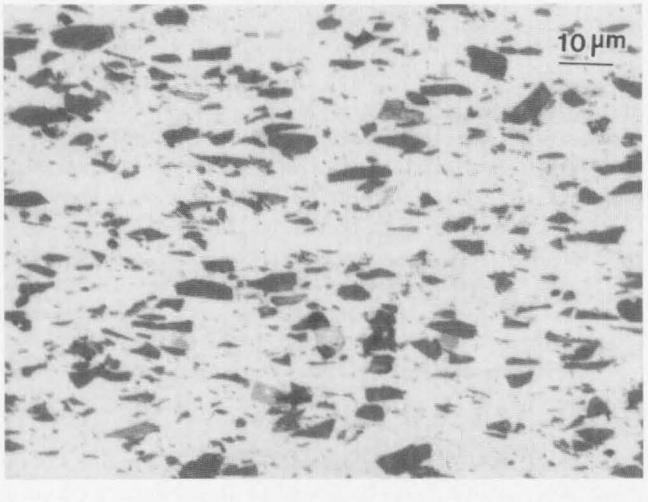

Fig. 2—Distribution of SiC_p in the composite processed in the PSN regime ($\dot{\varepsilon}$ = 5.6/s, T = 400 °C) after final extrusion to a total true strain of 5.67.

Following extrusion, the billets were either solution treated at 560 °C, or subsolvus annealed at 480 °C or 450 °C for 20 minutes, and water quenched. Each of these treatments had a twofold purpose: (1) to completely recrystallize the as-extruded billet and (2) to dissolve all or part of the existing matrix precipitates into the solid solution. Subsequently, samples of the composite were subjected to a number of different heat treatments, including artificial aging at 170 °C for 8 hours and natural aging for 9 months. Some of the completely solutionized samples were also subjected to a double aging treatment consisting of a 10-minute soak at 450 °C to precipitate some coarse, incoherent β (Mg_2Si) particles, followed by water quenching and subsequent aging for 8 hours at 170 °C in order to produce a fine disperison of β''/β' hardening precipitates. The various heat-treatment conditions and their designations are summarized in Table III.

Samples of the heat-treated composites were then tested in tension and mode I fracture with the extrusion direction as the loading axis. Tension tests were conducted on flat dog bone–shaped specimens with a gage length of 0.0254 m, and fracture toughness tests were conducted using compact tension (CT) specimens in compliance with either ASTM standard E-399-83, for determining K_{IC} (unstable fracture), or standard E-813-89, for determining J_{IC} (stable fracture). The J_{IC} data were subsequently converted into equivalent K_{IC} values using the formula $K_{IC} = \sqrt{J_{IC}E/(1-\nu)^2}$, where E and ν are the Young's modulus and Poisson's ratio of the DRA, respectively. For cases exhibiting stable fracture, the tearing modulus ($T = (E/\sigma_{ys}^2)dJ/da$), representing the crack propagation fracture toughness, was also calculated after fitting the J *vs* crack length (a) data with a straight line, in accordance with ASTM standard E-813-83. All the CT specimens had a nominal a_0/W value of 0.54 and had a thickness of either 0.0075 or 0.010 m.

Following mechanical testing, the composite samples were inspected using an optical microscope, scanning electron microscope (SEM), and transmission electron microscope (TEM). The TEM sample preparation method was similar to those reported elsewhere (*e.g.*, Reference 36). Following preparation of the TEM samples, they were observed in a TOPCON 002B TEM at an accelerating voltage of 200 kV.

The matrix precipitation behavior in some of the composite samples was also studied by a differential scanning calorimeter (DSC). For these experiments, 0.0015-m-thick disks of 0.0055-m diameter were electrodischarge machined from the as-processed billets, appropriately heat treated, and then scanned in a Perkin-Elmer Series 7 DSC at 10 K/min, from 300 to 833 K, in flowing nitrogen. Further procedural details of the calorimetric experiments are identical to those reported in Reference 36.

III. RESULTS

A. *Effect of Thermomechanical Process Conditions*

The optical micrograph in Figure 1 shows the distribution of SiC*p* in the composite matrix following the first extrusion step (true strain of 3.38). It is apparent that, despite the large process strain, some localized inhomogeneities in particulate distribution still remain in the microstructure. Figures 2 and 3 show the particulate distribution following the final extrusion step (true strain of 5.67) in the PSN and non-PSN regimes, respectively. By comparing Figures 2 and 3 with Figure 1, it is clear that the additional extrusion strain of 2.29 (beyond 3.38) results in appreciable further homogenization of the particulate distribution. However, the absence of any discernible difference between Figures 2 and 3 suggests that the particulate distribution is

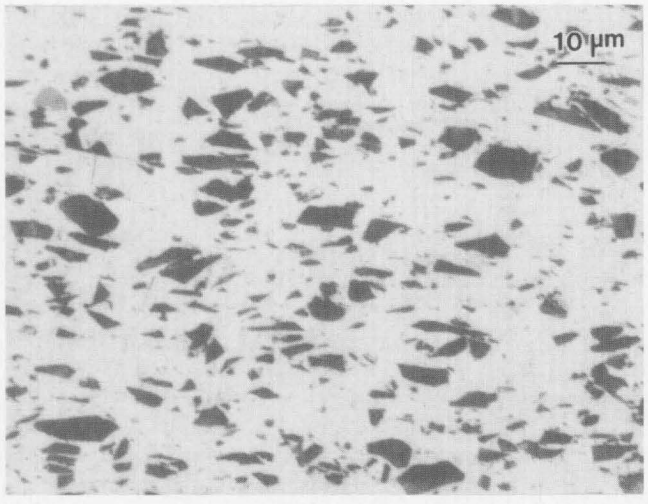

Fig. 3—Distribution of SiC_p in the composite processed in the non-PSN regime ($\dot{\varepsilon}$ = 0.6/s, T= 400 °C) after final extrusion to a total true strain of 5.67.

influenced primarily by the total process strain, with little apparent dependence on the processing route.

Despite the lack of any significant difference among the particle distributions in the composites extruded under the PSN, non-PSN, and intermediate states, the matrix microstructural details under these conditions were found to be quite different. Figures 4 through 6 show TEM micrographs of the three extruded materials (PSN, non-PSN, and intermediate states, respectively) following solution treatment at 560 °C. Figure 4(a) shows the typical microstructural appearance in the vicinity of two SiC particles for the sample processed under PSN conditions. Near particulates, the matrix grain size appeared to range from 2 to 4 μm, which is significantly smaller than the average SiC particle size (7 μm). The misorientation between adjacent grains was determined from the translation of the Kikuchi line center from the 000 spot in the [001] selected-area diffraction pattern (SADP) of adjacent grains, as well as the relative rotation of the Kikuchi patterns from these grains. This procedure, while not suitable for describing the grain-boundary character unambiguously, yields the tilt and rotation reorientations of adjacent grains relative to the [001] axis and is, therefore, suitable for comparing the relative misorientations of various boundaries. The approach is illustrated for one boundary in Figures 4(b) and (c), which show SADPs containing both spot and Kikuchi patterns from two adjacent grains in the material processed in the PSN regime. The translation of the Kikuchi line center from the 000 spot in Figure 4(c) corresponds to a relative inclination of 9.96 deg between the [001] plane normals of the two grains across the boundary, while the rotation of the pattern determined from comparison of the patterns in Figures 4(b) and (c) corresponds to an additional lattice reorientation of 20 deg. Most of the boundaries studied in the PSN material resulted in translations and rotations corresponding to lattice reorientations of 6 to 12 deg and ~10 to 20 deg, respectively. No dislocation structure could be resolved within such boundaries, which is consistent with the formation of high-angle boundaries during recrystallization. However, some low-angle boundaries with clearly discernable dislocation networks and unrecovered dislocations were also observed, as shown in Figure 4(d). In general, Kikuchi pattern translations suggested misorientations for such boundaries of 0.5 to 1 deg. In regions away from large SiC particles, somewhat larger grains, stabilized by small (0.1 to 0.2 μm) SiC particles which were deliberately added for this purpose,[37] were observed, as shown in Figure 4(c).

Figures 5(a) through (c) show bright-field TEM micrographs of the composite processed in the nonPSN regime. A significantly larger grain size of 6 to 10 μm, which is on the order of the interparticle spacing, is observed (Figure 5(a)). Characterization of the boundaries close to large SiC particles revealed pattern translations and rotations corresponding to lattice reorientations ranging from 8 to 14 deg and 10 to 20 deg, respectively. Thus, the apparent character of the boundaries close to large SiC particles is similar to that obtained by processing in the PSN regime, although the grain size in the non-PSN regime is larger. A close inspection of Figure 5(a) reveals several straight line–like features within the grain (indicated with arrows), which may be interpreted as surface slip steps, possibly produced by planar slip of screw dislocations in the TEM foil. Such slip lines have been noted in aluminum earlier[38] and are thought to be associated with the glide of several parallel coplanar dislocations with identical Burgers vectors. Indeed, a number of instances of planar dislocation arrays were observed in the non-PSN material in regions away from SiC*p*, as observed in Figure 5(b). This seems to suggest that in this material a limited number of slip systems are active, and when the mobile dislocations encounter a barrier, they pile up rather than cross-slip to other systems.

Figure 6(a) shows a bright-field TEM image of the material processed in the intermediate regime. The matrix next to the SiC particles is observed to be recovered into subgrains 2 to 5 μm in size, with clearly resolvable dislocation structures apparent within the subgrain boundaries. Figures 6(b) and (c) show two [001] SADPs from adjacent subgrains, illustrating the low-angle character of the boundaries for this processing condition; for this example, the pattern translation corresponds to a misorientation of 1.04 deg, with no additional contribution from pattern rotation. It was, thus, apparent that processing in the intermediate regime resulted in a recovered matrix microstructure with little or no recrystallization. However, the subgrain size in this case was found to be roughly similar to the grain size in the PSN state.

Figure 7 shows a plot of K_{IC} *vs* yield strength (σ_{ys}) for the composite in the -T6 condition after the initital extrusion step (ε = 3.38) and following final processing (ε = 5.67) in the PSN, non-PSN, and intermediate regimes. For reference, data for a 15 vol. pct Al_2O_3 particulate-reinforced 6061 Al composite, as a function of aging at 177 °C (from Reference 7), are also plotted in Figure 7. It is observed that, with increasing extrusion strain in the non-PSN regime (3.38 to 5.67), both strength and fracture toughness improve, this being attributable to increased uniformity of particle distribution with increasing process strain. It is also observed that processing to the same overall strain (ε = 5.67) in the intermediate regime results in an additional improvement in the strength-toughness combination over that for the non-PSN state, whereas processing in the PSN regime yields an even greater improvement. Since, as dis-

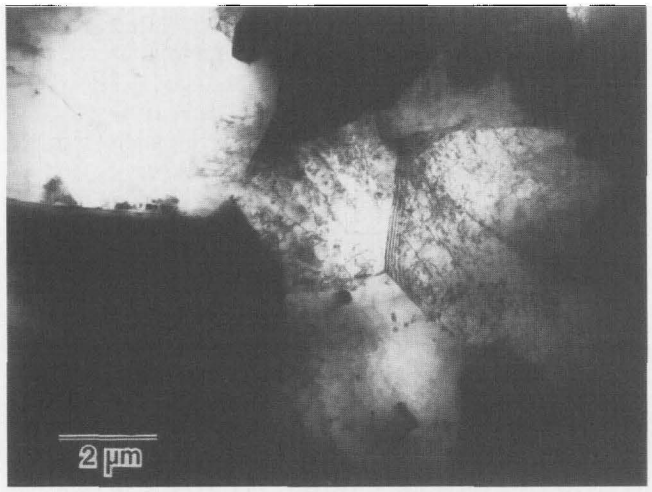

(a)

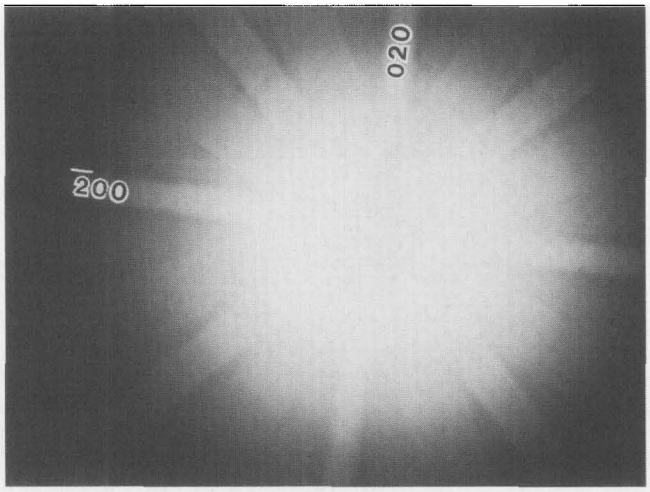

(b)

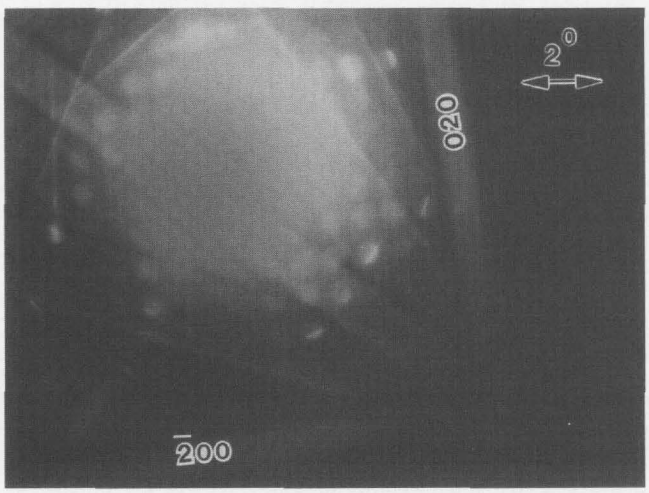

(c)

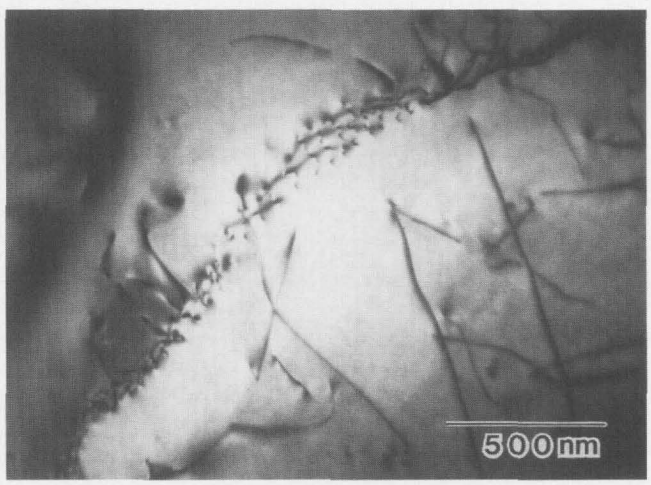

(d)

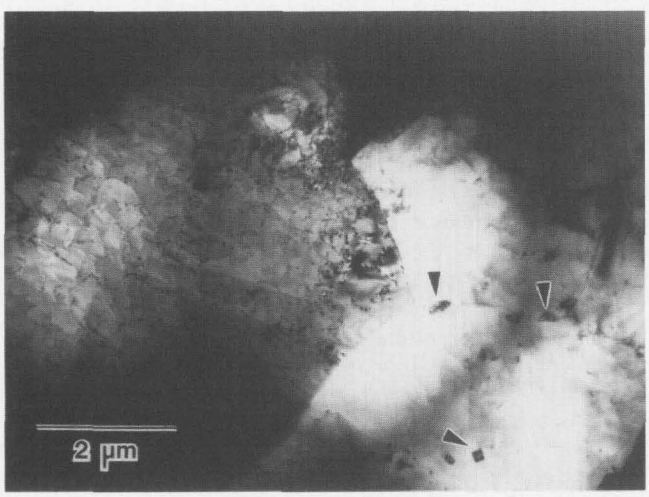

(e)

Fig. 4—(*a*) Bright-field TEM micrograph showing the typical matrix grain structure of the composite processed in the PSN regime in a region close to SiC_p. The grain size in such regions was ~2 to 4 μm. (*b*) SADP from one of the grains in (a), with $(\overline{B}) \equiv (\overline{z}) \equiv [001]$. The [001] spot pattern is obfuscated by the intensity of the Kikuchi pattern. (*c*) SADP from an adjacent grain with the same sample orientation as in (b), showing that the [001] zone axis is inclined to $(\overline{B})$ by 9.96 deg. The SADP from grain 2 is also observed to be rotated about $(\overline{z}) \equiv [001]$ by 20 deg relative to the SADP from grain 1. (*d*) A different region of the same sample showing low angle grain boundaries with clearly resolvable dislocation structures. These were typically observed in regions away from SiC*p*. (*e*) A micrograph showing evidence of grain size stabilization by fine SiC*p* (0.1 to 0.2 μm). Some of the SiC*p* are indicated by arrows.

cussed earlier in association with Figures 2 and 3, there is little discernible difference in the particulate distributions resulting from extrusion to the same total strain in different process regimes, any difference between the properties of the PSN, non-PSN, and intermediate states must be traceable to differences in the matrix microstructure (*i.e.*, grain size and substructure).

Figure 7 also shows the data for a monolithic aluminum alloy 6061 in the -T6 condition. It is noted that, in following processing to a true strain of 5.67 in the PSN regime, the 6092 Al-SiC*p* DRA is nearly as tough as the unreinforced 6061 Al (K_{IC} of 27 *vs* 29 MPa$\sqrt{m}$) while being 63 pct stronger (σ_{ys} = 450 *vs* 276 MPa) and 47 pct stiffer (E = 103 *vs* 70 GPa) than the unreinforced alloy in an equiv-

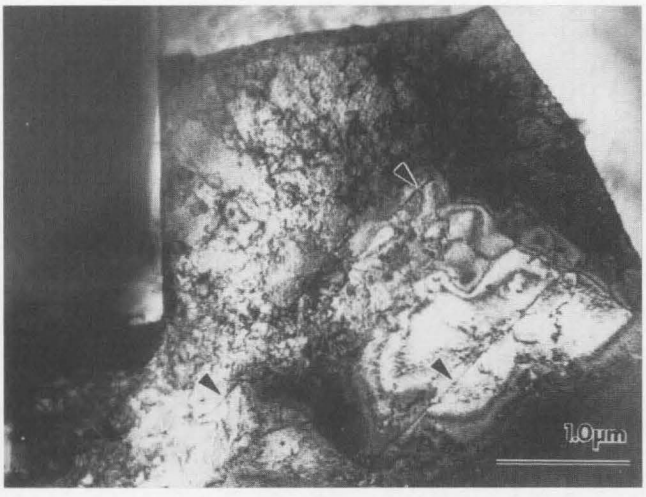

(*a*)

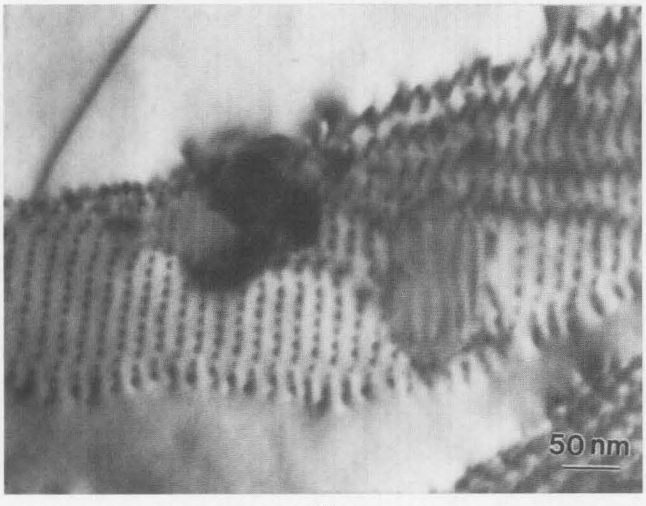

(*b*)

Fig. 5—(*a*) Bright-field TEM micrograph of the composite processed in the non-PSN regime, showing a larger grain size (~8 μm) than in the PSN condition. Several planar slip traces, indicated by arrows, are also observed. (*b*) A higher magnification micrograph of the non-PSN material showing a planar dislocation array. A number of instances of such arrays were observed in this material.

alent aging condition (-T6). It is to be noted that the alloy designations 6061 and 6092 refer to similar compositions, with the exception that 6092 has a higher allowable Cu concentration range (0.7 to 1.0 pct in alloy 6092 vs 0.15 to 0.4 pct for alloy 6061). The additional Cu in alloy 6092 does not contribute to precipitation hardening, but serves as a grain refiner. This, in conjunction with the additional grain refinement resulting from the submicron-sized SiC*p* added to the present DRA, results in the higher observed strength levels relative to the 6061 Al-matrix composite of Reference 7. It is also noteworthy that the Al_2O_{3p}-6061 Al DRA of Reference 7 was processed to a total true strain of only 2.87 starting from the as-cast state and is, therefore, expected to have a relatively less homogeneous particulate distribution than the material of the present study. This would have resulted in a greater degree of strain localization during deformation, accounting for the significantly reduced strength and toughness levels observed in Reference 7 as compared to the present material.

The data from Reference 7, plotted in Figure 7, suggest that the only way to increase the fracture toughness of the DRA beyond that available in the peak-aged (-T6) condition is to leave the matrix in an UA state. However, this would result in continuous evolution of the microstructure (and, hence, properties) during subsequent service and is, therefore, unacceptable. Thus, although processing to large strains in the PSN regime followed by peak aging, as outlined previously, yields desirable results, further increase in the intrinsic fracture toughness is not feasible using conventional heat treatments. Therefore, the effect of a subsolvus solution anneal (SA), comprised of 20 minutes at 450 °C followed by water quenching after extrusion, was studied. During this subsolvus SA, PSN of recrystallization occurs in the presence of coarse β particles, which are envisioned to provide Zener drag on the migrating recrystallized grain boundaries, thereby limiting grain growth. Subsolvus solutionization also allows control of the amount of solute in solution and, therefore, of composite strength. Finally, following subsolvus solutionization, the SA microstructure is expected not to be conducive to Guinier–Preston (GP) zone formation and should, therefore, be minimally susceptible to natural aging.

Figure 8 shows a bright-field TEM micrograph of the matrix region of the sample extruded under PSN conditions, followed by solution annealing for 20 minutes at 450 °C. As expected, the microstructure reveals relatively coarse incoherent β particles within the grains, with additional β particles clearly visible at the grain boundaries. The matrix grain size of this material was found to be similar to that of the fully solutionized sample following processing in the PSN regime (2 to 4 μm), and the grain boundary misorientations were also found to be similar. A rough calculation based on the Zener drag model shows that 20-nm-sized incoherent particles should stabilize a grain size of about 2.5 μm, which is in the range of grain sizes observed in the material. This suggests that the β particles indeed exert a pinning effect on boundary migration during recrystallization. Thus, the primary effects of the 450 °C SA treatment are (1) to limit grain growth and (2) to deplete the matrix of dissolved solute and, thereby, to reduce its strength. An interesting point to note in this material was the near-absence of interfacial precipitates, as has often been observed in OA microstructures (*e.g.*, References 2 and 36).

Figure 9 shows the force *vs* crack opening displacement plots for the composite processed in the PSN regime, following the -T6 and SA treatments. In the -T6 condition, the material displays unstable crack propagation, whereas in the SA condition, it shows slow, stable crack extension. The crack initiation fracture toughness (J_{IC}) was determined to be 13 kJ/m^2, which is equivalent to a J_{IC} of 38 MPa$\sqrt{m}$. This is plotted in Figure 7, along with the corresponding σ_{ys} value. It is clear that a substantial increase in the intrinsic fracture toughness is associated with the SA treatment, albeit accompanied by a large drop in σ_{ys}. Further, the crack propagation fracture toughness of the SA material, represented by the tearing modulus T, was determined to be 31, which is nearly one of magnitude larger than those reported previously for DRA materials in conventionally heat-treated conditions.[6]

Figures 10 through 12 provide insight into the roles of extrusion and heat-treatment conditions on the fracture

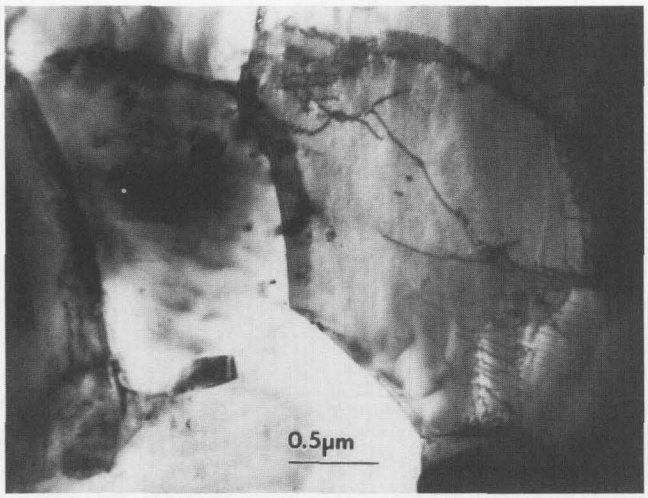

(*a*)

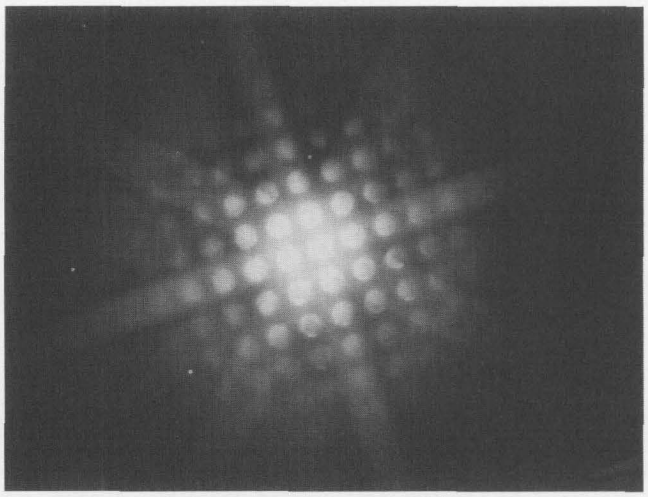

(*b*)

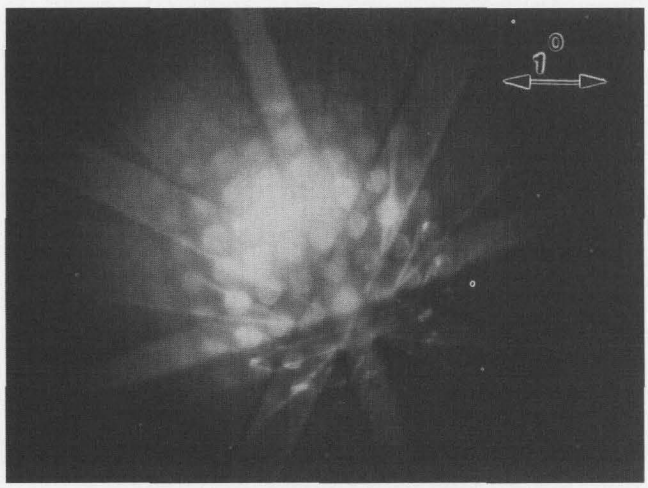

(*c*)

Fig. 6—(*a*) Bright-field TEM micrograph of the composite processed in the intermediate regime, showing a fine subgrain structure. A majority of the boundaries in this condition had resolvable dislocation structures, indicating a recovered microstructure. (*b*) SADP from one of the subgrains in (a), with $(\overline{B}) \equiv (\overline{z}) \equiv [001]$. (*c*)SADP from an adjacent subgrain with identical sample orientation as in (b), showing that the [001] zone axis is inclined to $(\overline{B})$ by 1.04 deg. Comparison of this SADP with that in (b) reveals no rotation about [001].

mechanisms in the experimental DRA. Figures 10(a) and (b) show SEM fractographs of the DRA after tension testing, following processing in the PSN and nonPSN regimes, respectively. Both samples were fully solution treated and artificially aged (-T6 treatment) prior to testing. In both cases, evidence of widespread particle fracture is observed, suggesting that crack initiation occurs by void nucleation at cracked particles and is followed by fracture of the matrix. Although both samples show generally ductile fracture characteristics, the details of matrix fracture are significantly different. Following processing in the PSN regime, the matrix between fractured particles fails almost entirely by microvoid nucleation and coalescence. After processing in the non-PSN regime, however, significant evidence of quasi-cleavage faceting is observed, in addition to ductile dimples. This difference in the matrix fracture mechanism, which is responsible for the difference between the observed fracture toughnesses of the two states, should be attributable to the difference in the matrix grain and dislocation structure, since the particulate distribution and the matrix precipitate structure in both samples were very similar and will be discussed later.

Figures 11(a) and (b) show optical micrographs of the crack-tip region of sectioned CT specimens of the composite processed in the PSN regime in the -T6 and 450 °C SA conditions, respectively. Figures 12(a) and (b) show SEM fractographs of the same two samples following separation of the two halves of fractured CT specimens. As observed in Figure 11(a), in the -T6 specimen, damage is observed to accumulate significantly ahead of the primary crack front by cracking of large particles and particle/matrix fracture within clusters of small particles. Figure 12(a) reveals fractured particles within the majority of large dimples on the fracture surface in the -T6 sample, suggesting that crack propagation occurs by fracture of particles followed by ductile fracture of the adjoining matrix. In the 450 °C SA sample, however, no damage is observed ahead of the primary crack front (Figure 11(b)). Although some particle cracking is still observed both in the fracture profile (Figure 11(b)) and in the fractograph (Figure 12(b)), it is clear from Figure 12(b) that the majority of the microvoids (dimples) do not contain cracked particles. Further, it is noted that the microvoids in Figure 12(b) are significantly larger and deeper than those in Figure 11(b), accounting for the large difference in strength and toughness observed in Figure 7. It is, thus, clear that, in the hard condition (-T6 treatment), the fracture of the present DRA is particle controlled, whereas in the soft condition (SA treatment) it is predominantly matrix controlled.

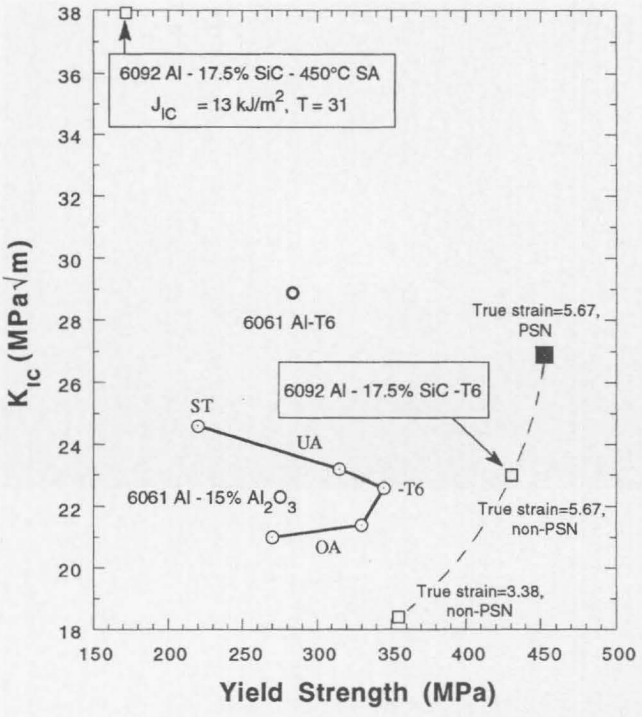

Fig. 7—Plot of fracture toughness *vs* yield strength data for SiC*p*-6092 Al composite in various conditions and a monolithic 6061 Al in the -T6 condition. For comparison, data for an Al_2O_3-6061 Al composite as a function of artificial aging at 177 °C[7] are also shown. ST, UA, and OA represent the solution-treated, underaged, and overaged conditions, respectively.

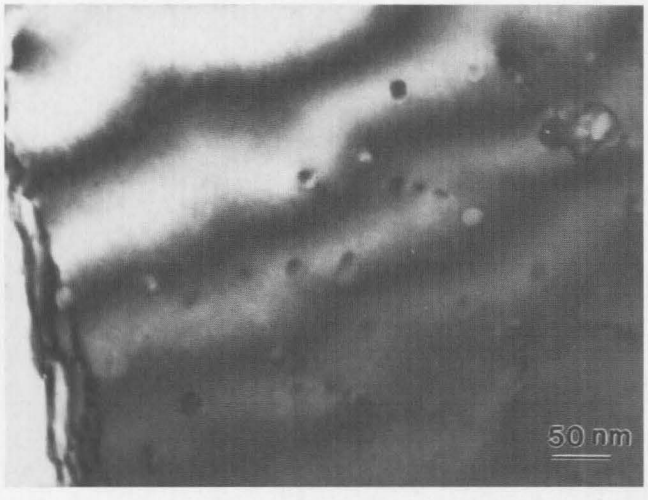

Fig. 8—Bright-field TEM micrograph of the matrix of the material processed in the PSN regime, followed by subsolvus solution annealing at 450 °C for 20 min (450 °C SA). Several 25- to 30-nm-sized incoherent β precipitates are observed within the grain, as well as at the grain boundary.

B. *Effect of Heat Treatment/Aging Conditions*

The above data clearly demonstrate that DRA composites are not inherently brittle and, when appropriately processed, can yield a stable microstructural condition which is soft and highly tough. This suggests that, by a suitable combination of processing and heat-treatment steps, it should be possible to produce an array of conditions ranging from hard and brittle (-T6 condition) to soft and tough (SA condition), thereby enabling optimization of the strength-toughness combination in DRA.

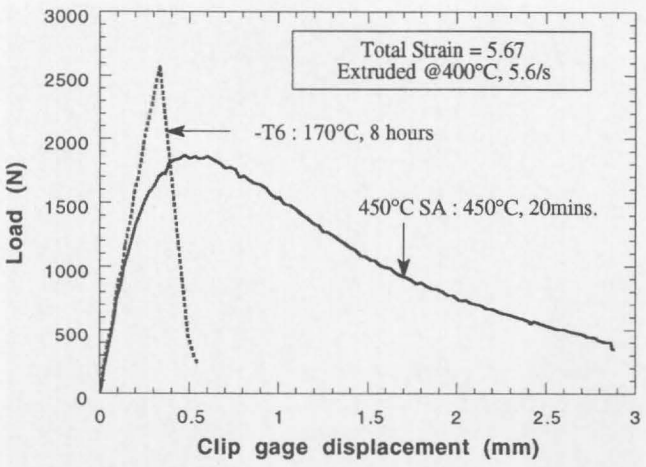

Fig. 9—Force *vs* crack opening displacement plot for the Sicp-6092 Al following the -T6 treatment and after the 450 °C SA treatment. In the -T6 condition, the material shows brittle behavior, whereas after the subsolvus anneal, it is very tough and shows slow, stable crack extension.

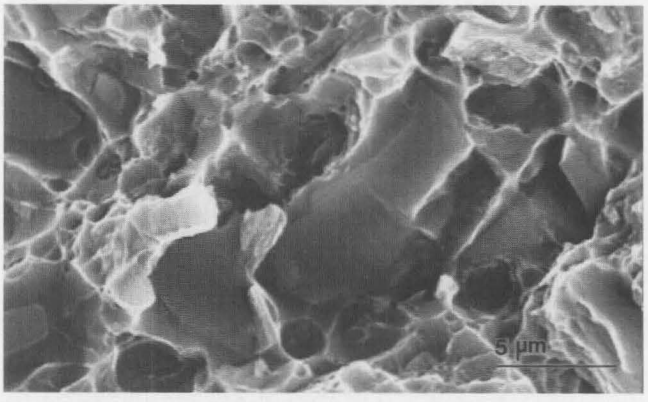

(*a*)

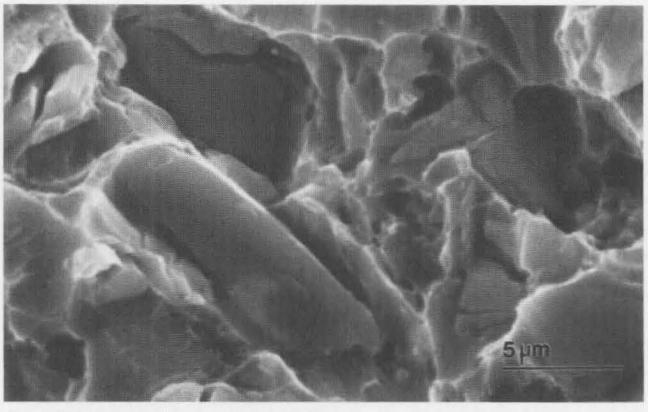

(*b*)

Fig. 10—SEM fractographs of the composite after tension testing, following processing in (*a*) the PSN regime and (*b*) the non-PSN regime, and heat treatment to the -T6 condition. Both the PSN and non-PSN states show particle fracture, but the matrix in the PSN state shows ductile dimpling, whereas the matrix in the non-PSN state shows quasi-cleavage in conjunction with ductile fracture.

Figure 13 shows DSC scans of the DRA after (1) full solution treatment at 560 °C, (2) SA at 450 °C, and (3) isothermal aging at 170 °C for 8 hours following a 450 °C

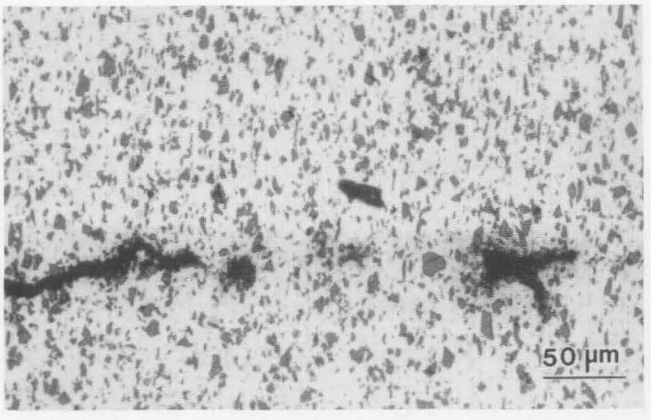

(*a*)

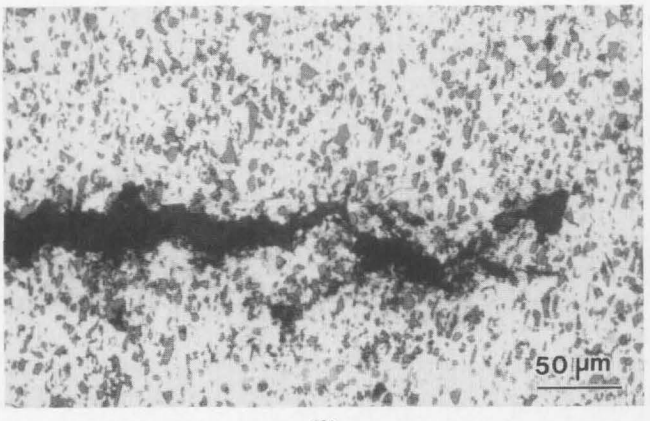

(*b*)

Fig. 11—Optical micrographs of the crack tip region of sectioned compact tension specimens of the PSN material, heat treated to the (*a*) -T6 and (*b*) 450 °C SA conditions. In the -T6 condition, damage is observed to occur ahead of the crack tip *via* fracture of large or clustered particles.

SA treatment. The various exotherms associated with the DSC thermogram of precipitation-hardenable Al-Mg-Si (6*xxx* series Al) alloys were characterized in detail earlier[39,40] and are indicated in Figure 13. It is apparent that the 450 °C SA treatment suppresses vacancy-Si clustering during the DSC scan, possibly because of the reduced levels of quenched-in vacancies and excess free solutes in this condition as compared to the fully solution-treated condition. This results in the disappearance of the GP-I zone precipitates in this condition, thereby reducing its propensity toward natural aging. Despite the substantially reduced levels of solute concentration in the SA condition, however, it is observed that the volume fraction of precipitates obtainable during a subsequent DSC scan (or aging treatment) is still considerable. Isothermal aging at 170 °C is observed to precipitate all possible β'', as well as a significant amount of β', thereby allowing appreciable futher hardening following the SA treatment. Based on the this, it seems possible to design aging treatments following a subsolvus anneal with the aim of optimizing the strength-toughness relation in DRA.

Figure 14 plots the K_{IC} *vs* yield strength data for the experimental DRA, under various heat-treatment conditions, for each of the three process conditions (PSN, non-PSN, and intermediate). All the samples tested had total true extrusion strains of 5.67 and, therefore, as discussed

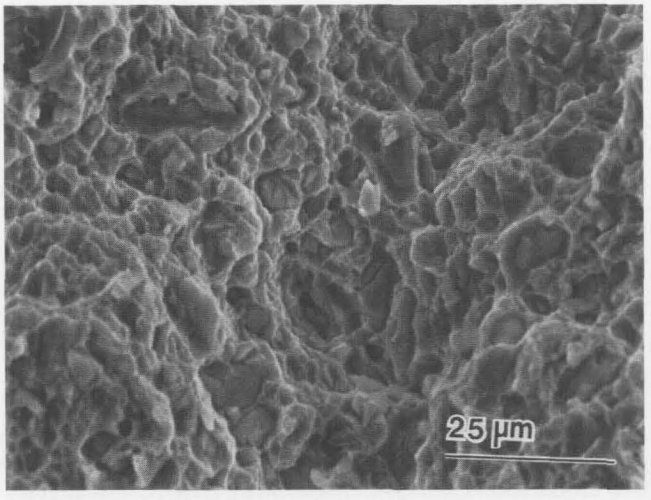

(*a*)

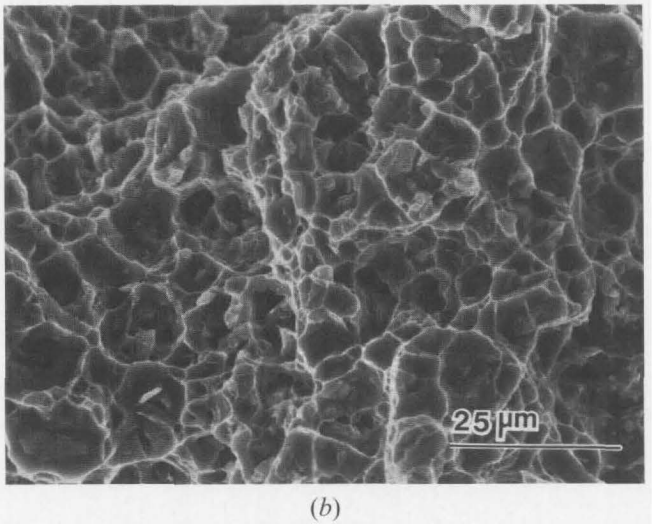

(*b*)

Fig. 12—SEM fractographs of the PSN composite, heat treated to the (*a*) -T6 and (*b*) 450 °C SA conditions. The fracture surface of the -T6 sample is characterized by numerous fractured SiC particles and dimples associated with ductile matrix failure. In the 450 °C SA condition, there is little evidence of particle fracture, and the matrix dimples are larger and deeper, suggestive of the increased toughness of the material.

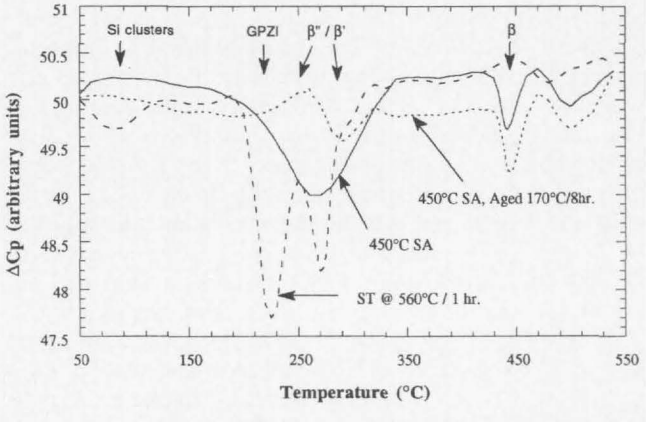

Fig. 13—DSC plot of the composite in the non-PSN state after (1) a full solution treatment (1 h at 560 °C), (2) subsolvus annealing (20 min at 450 °C), and (3) 450 °C SA followed by isothermal aging at 170 °C for 8 h. The heating rate in each case was 10 °C/min.

earlier, the differences in the strength-fracture toughness combinations in Figure 14 are entirely attributable to differences in the matrix microstructure. Data for a peak-aged (-T6 condition) monolithic 6061 Al alloy are also plotted in Figure 14. Each point in the that plot is based on the results of two fracture toughness tests and one tensile test.

Three features of Figure 14 are of interest. First, the data demonstrate that it is possible to produce a series of stable microstructural conditions ranging in strength-toughness combinations between the soft (and tough) 450 °C SA condition and the strong (and relatively brittle) -T6 condition. Second, it is clear from a comparison of the data for the composite with those for monolithic 6061 Al that it is possible to produce DRA with better strength *and* toughness than the monolith, while obtaining a significant stiffness advantage. And finally, it is apparent that, while the extrusion condition has some effect on the strength-toughness combination of DRA at the extremes of strength levels, in the middle range, the properties of the composite are dependent primarily on the heat-treatment condition (*i.e.*, matrix precipitate structure) with no perceptible effect on the process condition. At the high- and low-strength ends (the -T6 and 450 °C SA conditions), processing in the PSN regime improves the toughness relative to the non-PSN state, as discussed earlier. The intermediate state produces a toughness close to that of the PSN state in the -T6 condition, but near that of the non-PSN state in the SA condition. In the intermediate-strength range, the PSN, the non-PSN, and the intermediate states produce strength-toughness combinations which are very close to each other. This suggests that the properties of DRA (at least, those with a 6*xxx* Al matrix) may be largely optimized by heat treatment only, except at the high-strength end, where it is beneficial to process the composite in the PSN regime.

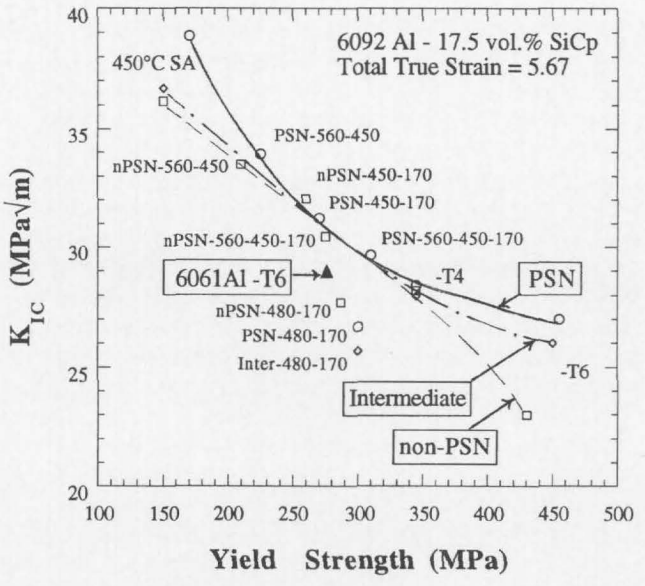

Fig. 14—Plot of fracture toughness *vs* yield strength of the composite under various heat treatment conditions for the PSN, intermediate, and non-PSN states. For comparison, data for unreinforced 6061 Al in the -T6 condition are also shown. All data points correspond to a total process strain of 5.67.

IV. DISCUSSION

The first reference to the effect of grain size on fracture stress was by Petch,[41,42] who noted that the fracture strength (σ_f) should increase with decreasing grain size. Later, Heslop and Petch[43] showed that the ductile-to-brittle transition temperature in steels decreased systematically with decreasing grain size, suggesting that the toughness increases with grain refinement. However, there is still some controversy about the impact of grain size on fracture toughness, as denoted by the energy required to propagate a crack (G_c, the critical energy release rate, or K_c, the critical stress intensity factor), particularly in the case of ductile fracture. Based on the Bilby–Cottrell–Swinden (BCS) model of the crack-tip plastic zone,[44] the fracture toughness $G_c = 4\sigma_0 r_y/\pi\mu$, where σ_0 is the flow stress, r_y is the plastic zone size, and μ is the shear modulus. As suggested by Li and Li,[28] a range of grain size (d) dependencies of G_c may be inferred from the previous relationship, depending on the specific assumption made. This ranges from $G_c \propto d^{-1}$ (*i.e.*, $K_c \propto d^{-1/2}$), when r_y is independent of the grain size ($r_y > d$), to G_c (and K_c) being independent of d when $r_y \propto \sigma_f^2$ ($r_y \ll d$). Indeed, as noted by Li and Li, experimental data[23 26] generally agree with the relation $K_c \propto d^{-1/2}$, although an increase in fracture toughness with increasing grain size has been noted when $d > r_y$.[28,45] Analytic formalisms developed by Li and Li for crack-tip dislocation distributions indicate that the fracture toughness depends not only on the grain size (*i.e.*, crack tip–to–barrier distance), but also on the relative magnitudes of lattice friction and grain-boundary strength. For grain-boundary strength >> lattice friction, they[28] suggested a reciprocal square-root grain-size dependence of G_c (*i.e.*, $K_c \propto d^{-1/4}$). When grain-boundary strength ~ lattice friction, G_c (and K_c) can be deduced to be independent of d based on their analysis. In the previous discussion, the grain-boundary strength is defined as the critical grain-boundary stress concentration required to punch dislocations into the adjacent grain and may, therefore, be expected to depend on the grain-boundary misorientation. Based on this, it may be surmised that, depending on the type of grain boundaries present, the fracture toughness may either be independent of grain size or may have a small but significant dependence on the grain size.

Although the statistics of grain size measurement in the TEM are difficult to assess, careful comparison of matrix regions with qualitatively similar particulate distributions in the three extrusion conditions (designated as PSN, non-PSN, and intermediate) suggest that different process conditions produce significant differences in both matrix grain size and substructure. Because of the high strain rate and relatively low extrusion temperature used in the PSN regime (5.6/s and 400 °C, respectively), relatively little diffusional strain relaxation (climb-controlled recovery) occured during extrusion, resulting in the storage of substantial strain energy to cause PSN of recrystallization during subsequent heat treatment. This process, as the results show, produces small grains next to the particles, with high-angle boundaries having both tilt and twist misorientations. Away from particles, where the plastic strains induced during processing are lower, some recovered structures were also observed. In the non-PSN regime, the low strain rate (0.6/s) allows some recovery next to particles despite the low processing temperature (400 °C), resulting in little PSN

of recrystallization and, consequently, a larger grain size. In the intermediate regime, the high temperature (450 °C) allows substantial recovery processes to be active despite the high strain rate and is evidenced by the presence of fine subgrains with low-angle boundaries and dislocation substructures everywhere in the matrix.

In a recovered structure with primarily low-angle grain boundaries, the grain-boundary strength (τ_{gb}) is expected to be close to the lattice friction (τ_f),* and, therefore, such a material should show little grain-size dependence on fracture toughness. In the vast majority of Al-matrix composites processed at high temperatures (450 °C and above), this is likely to be the situation, irrespective of the extrusion rate. Indeed, several previous TEM studies have noted that the matrix next to reinforcements is typically characterized by a well-defined subgrain structure containing a high dislocation density—a structure representative of a recovered condition (*e.g.*, References 13 and 46). In such a situation, therefore, microstructural refinement is not expected to yield dividends in terms of fracture toughness. Recrystallization and the presence of high-angle boundaries (with high τ_{gb}) are, therefore, crucial in obtaining fracture toughness improvements by microstructural refinement. However, as discussed previously, the effect of grain size on fracture toughness is dependent of the relative magnitudes of τ_{gb} and τ_f and is, therefore, not straightforward. For instance, it is observed from Figure 14 that when the matrix is soft (*e.g.*, 450 °C SA), the PSN state produces a significantly better fracture toughness than the non-PSN state. However, in the intermediate-strength regime, both states display similar toughnesses, despite the difference in grain size and the similarity in the nature of the grain boundaries. This may be partly attributed to the increase in τ_{gb} in the intermediate-strength regime, which desensitizes fracture toughness to the grain size.

Figure 14 shows that, with a continued increase in the matrix strength level (by precipitation hardening to the -T6 condition), the PSN material once again displays a greater toughness than the non-PSN material. This, however, appears to be due to a different reason. As noted in Figures 10(a) and (b), the matrix in the non-PSN state showed significant evidence of quasi-cleavage fracture as opposed to primarily ductile dimpling in the PSN material. Quasi-cleavage fracture in ductile materials is usually thought to be promoted under conditions that impede plastic flow.[47] It is likely that this increased predilection toward cleavage of the non-PSN material relative to the PSN condition is due to the constraint to matrix plastic flow imposed by the generation of large hydrostatic stresses in the interparticle regions because of slip localization on certain systems. This is evidenced by the presence of straight slip lines and planar dislocation arrays in the non-PSN material, suggesting the inhibition of cross-slip processes, possibly due to textural effects. The increased rate of work hardening (RWH) in the non-PSN material relative to the PSN material in the -T6 state is further evidenced by Figure 15, which plots RWH for both materials as a function of the proportional limit–normalized true flow stress (σ/σ_0) following the start of plastic flow during tensile testing. The initial decrease in RWH with increasing σ/σ_0 is attributable to the progressively accelerating kinetics of cross-slip–induced recovery processes, whereas the final region of small, constant RWH represents the situation where the kinetics of hardening processes are balanced by those of the recovery processes.[19,48] It is apparent that, while this balance is reached at a σ/σ_0 value of ~1.15 in the PSN condition, it is reached at around $\sigma/\sigma_0 \sim 1.6$ in the non-PSN material, which is close to the fracture stress of the material. This confirms that recovery processes are relatively slow in the non-PSN material, allowing rapid buildup of tensile triaxiality in the matrix during deformation and, thereby, promoting localized cleavage in the matrix between particles, as observed in Figure 10(b). A point to note is that, following fracture of some of the particles in a given plane, the hydrostatic constraint in the matrix is expected to be partially relieved. Yet, in the non-PSN material, the matrix shows evidence of quasi-cleavage failure. This suggests that, even following fracture of some of the surrounding particles, the constraint to plastic flow in the interstitial matrix is sufficient to make the matrix flow stress comparable to the cleavage stress in the non-PSN -T6 material. In the PSN -T6 material, on the other hand, the higher rate of recovery lowers the constraint, allowing plastic flow and fostering ductile fracture.

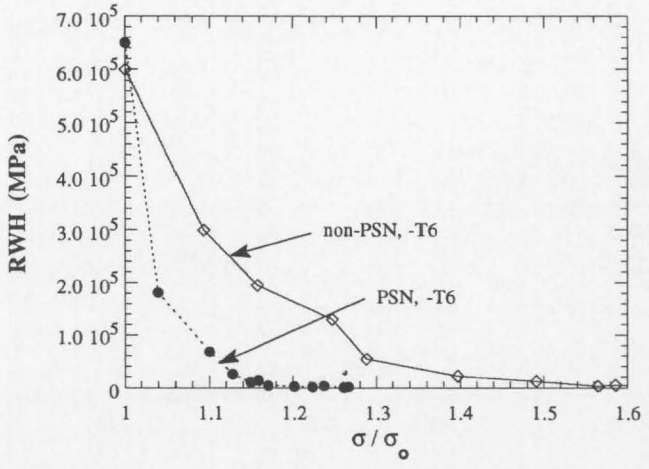

Fig. 15—Variation of the RWH as a function of the true flow stress normalized by the proportional limit (σ/σ_0) during plastic deformation of the composite in the -T6 state.

Figure 16 plots the RWH *vs* σ/σ_0 for the PSN and non-PSN states in the -T4 condition. Unlike in the -T6 condition, the RWH is observed to reach constancy in both materials at similar σ/σ_0 values (~2.1 for PSN and 2.3 for non-PSN), indicating relatively little difference between the matrix recovery rates in the two materials. In the -T4 condition, the matrix flow stress is significantly lower than in the -T6 condition, and it is likely that the mechanism responsible for inhibiting recovery processes in the -T6 condition is unable to provide sufficient plastic flow constraint to the matrix in the -T4 state to make the flow stress comparable to the cleavage stress. Indeed, the fractured -T4 sample exhibited only ductile fracture of the matrix between particles, with no evidence of quasi-cleavage. This, coupled with the fact that the lattice friction (τ_f) in the -T4 state is large enough relative to τ_{gb} to make the fracture toughness relatively insensitive to grain size, explains the absence of any perceptible difference between the fracture

*Here, the term τ_f is considered to incorporate the effects of all intragrain strengthening mechanisms such as the Peierl's potential, dislocation density, solute atoms, and precipitates.

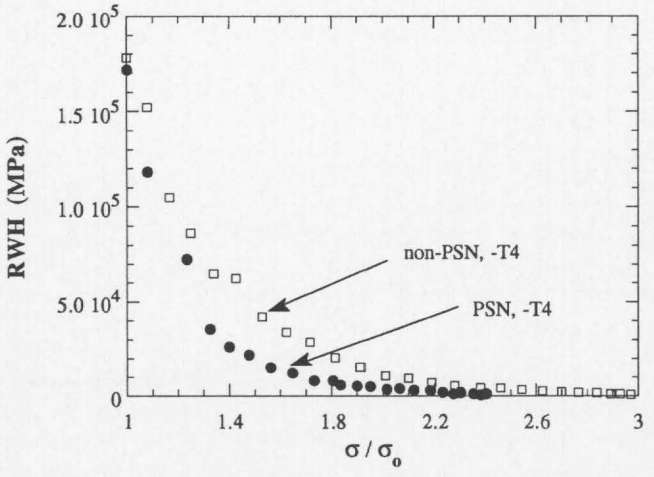

Fig. 16—Variation of the RWH as a function of the true flow stress normalized by the proportional limit (σ/σ_0) during plastic deformation of the composite in the -T4 state.

toughnesses of the PSN and non-PSN materials in the -T4 condition.

Figure 14 also indicates that, while the intermediate sample has a fracture toughness close to that of the non-PSN sample in the 450 °C SA condition, it displays a toughness close to that of the PSN sample in the -T6 condition. Thus, even when τ_f is low (*e.g.*, in the 450 °C SA condition), the intermediate state derives little benefit in K_{IC} relative to the non-PSN condition, despite its small subgrain size. This is because in this material, most of the boundaries have very low misorientation and, consequently, have a low τ_{gb}, thereby obliterating any advantage of having a finer microstructure than that of the non-PSN material. In the -T6 condition, the intermediate material showed predominantly ductile matrix failure, just like the PSN material, thus demonstrating no evidence of limited slip system operation. This accounts for the increased toughness observed in the intermediate material relative to the non-PSN material. Since, as discussed earlier, at this strength level the grain boundaries play a very small role in determining fracture toughness, the PSN and intermediate materials display similar K_{IC} values despite the difference in grain-boundary misorientation.

It is clear from the previous discussion that microstructural aspects besides grain size play a significant role in determining the relative strength-toughness combinations of the DRA processed under different conditions. A fine microstructure is beneficial with respect to the fracture toughness, as long as the grain boundaries are highly misoriented and $\tau_f \ll \tau_{gb}$. With increasing τ_f, the benefit of grain refinement decreases, and, for the high-strength matrix (-T6), it appears that the higher toughness observed in the PSN material relative to the non-PSN material is predicated on the dislocation substructure and its influence on the work-hardening behavior and matrix fracture mechanism. Further work is needed in order to understand the basis for the difference in matrix flow behavior in materials processed in different $\dot{\varepsilon}$-T regimes, in terms of the constituent dislocation structures, and to design experiments aimed at separating the roles of grain size and dislocation substructure in fracture toughness.

On the basis of the difference in fracture mechanisms in the -T6 and 450 °C SA conditions (Figures 11 and 12), it is apparent that the fracture path and mechanism can differ drastically depending on the matrix flow behavior. Whereas in a hard matrix (-T6 condition) the crack propagates by fracture of particles and matrix damage initiation within particle clusters followed by crack linkage through the matrix by ductile (or a combination of ductile and quasi-cleavage) fracture, in a soft matrix (the 450 °C SA condition) the crack propagates predominantly through the matrix with very limited particle fracture. In the -T6 condition, the matrix flow stress is high enough so that the fracture strength of some of the particles is reached by the time the matrix starts yielding. With an increasing crack-tip stress intensity fractor, the plastic zone size increases, as does the number of cracked particles within the plastic zone. This results in the transfer of stress from the fractured particles to the adjacent matrix, which, in the absence of the ability to work-harden substantially, is unable to support the additional stress when the local volume fraction of cracked particles reaches some critical value. Thereupon, the matrix between the cracked particles fails, resulting in overall propagation of the crack. On the other hand, in the SA condition, the matrix, which is very soft, flows and fails without the matrix flow stress ever reaching a high enough level for the particles to get loaded to their fracture stress, contributing to a predominantly matrix-controlled fracture and a correspondingly high fracture toughness. It is, thus, apparent that there are at least two alternative approaches to the production of a desirable combination of strength and fracture toughness in DRA. First, the matrix condition may be selected to be hard enough to permit loading of the reinforcement particulates, but soft enough to preclude premature particle fracture, so that the failure is matrix controlled. Alternatively, the matrix should have a high work hardening rate, so that, following particle fracture, it can take up the stress shed by the cracked particles and, thereby, delay strain localization and crack extension. The first condition may be satisfied by leaving the matrix in a slightly UA condition, with the risk of continued natural aging during use. The second condition may be satisfied by heat treating the matrix to produce a dispersion of incoherent precipitates, but with the potential risk of triggering a third fracture mechanism—interface-controlled fracture due to precipitate segregation at particle-matrix interfaces—and the associated drop in fracture toughness, as often observed in OA structures (*e.g.*, Reference 2). The results of this study suggest that a multistep heat treatment following deformation processing may be the most suitable approach. Such a heat treatment would consist of (1) a solutionization-*cum*-annealing treatment following deformation processing in order to recrystallize the matrix and dissolve the requisite amount of solute; (2) a high-temperature aging treatment to produce some incoherent precipitates, for an increased work hardening rate; and (3) a fine dispersion of coherent/semicoherent precipitates, optimizing the flow stress. Indeed, as demonstrated in this study using the -450-170 and -560-450-170 treatments (refer to Table III for nomenclature), an array of strength-toughness combinations may be produced by following the general approach outlined previously. The -480-170 treatment, where the SA treatment was conducted at 480 °C, displayed relatively low toughness values in all cases because of the formation of

coarse β platelets at the SiCp-matrix interface, which resulted in a fracture-mode transition to interface failure.

Finally, the present study seems to suggest that processing in the PSN regime, with the associated effects on matrix grain size and dislocation substructure, is beneficial with regard to fracture toughness only at the high and low extremes of strength levels. In the intermediate-strength regime, the differences due to different deformation processing routes are negligible as long as the total process strain (which determines the particulate distribution) is constant. Therefore, it appears that, except at the high- and low-strength ends, the properties of the DRA (at least the one studied here) may be optimized solely by post-processing heat treatments.

V. CONCLUSIONS

It was shown previously that, when processed appropriately, a *6xxx* Al-matrix DRA can display better stiffness, strength, *and* fracture toughness than the commercial aluminum alloy 6061 in the peak-aged condition.

It was found that the strength-fracture toughness combination in DRA depends strongly on both the particulate distribution and the matrix microstructural condition. The particulate distribution was found to be primarily a function of the total deformation processing strain, whereas the matrix microstructure, as expected, depends on both the process strain and the processing route. Thus, varying the processing route while keeping the total strain constant allows the separation of the effects of particulate distribution and matrix microstructure on properties.

Refinement of the matrix grain size *via* processing in the PSN regime appeared to be beneficial to the fracture toughness when the matrix is in a soft solution-annealed state or in the peak-aged condition. In the intermediate-strength regime, grain size control was found to not have much impact on properties. These effects were attributed to (1) the decreasing grain size dependence on fracture toughness at increasing τ_f/τ_{gb} ratios and (2) substructural differences accompanying grain size differences due to processing in different $\dot{\varepsilon}$-T regimes, which apparently result in differences in dislocation activity and, therefore, the plastic flow behavior of the matrix and the resultant fracture toughness.

A number of unconventional heat treatments were successfully explored with the objective of optimizing the strength-fracture toughness combination in DRA without resorting to an UA (*i.e.*, naturally age-hardenable) matrix microstructure. In general, it appears that the microstructural conditions conducive to improved fracture toughness are (1) a homogeneous particulate distribution fostered by processing to large total strains, (2) a small matrix grain size induced by PSN of recrystallization, (3) a high grain-boundary misorientation, (4) the presence of fine reinforcement particulates or coarse incoherent precipitates, to stabilize grain size during annealing *via* the Zener drag effect, and (5) a mixture of incoherent precipitates and coherent hardening precipitates in the matrix, to result in optimal flow stress and work hardening behavior.

Finally, the results indicate that, for a given total process strain, the effect of the processing route on the matrix flow properties and, hence, on the properties of the composite is appreciable only at the very high- and very low-strength regimes. At least for the present material, the processing route had little impact on properties in the intermediate-strength regime, where the properties seem to be dominated by the matrix precipitate state rather than by processing-induced microstructural variations.

ACKNOWLEDGMENTS

This research was supported by the United States Army Research Office, with Dr. W. Simmons as contract monitor and Dr. E. Chin of Army Research Laboratory as technical liaison, and the Summer Research Program of the United States Air Force Office of Scientific Research, with Dr. D. B. Miracle as technical monitor. Partial support from the Wright Materials Laboratory, with Dr. B. Maruyama as contract monitor, is also acknowledged. The authors thank Mr. Mark van den Bergh, DWA Composites, for supplying the experimental material gratis. One of the authors (ID) also gratefully acknowledges the assistance of, and many helpful discussions with, several colleagues at the Wright Materials Laboratory, especially Drs. B.S. Majumdar, V. Seetharaman, and S. Krishnamurthy.

REFERENCES

1. R.H. Jones, C.A. Lavender, and M.T. Smith: *Scripta Metall.*, 1987, vol. 21, pp. 1565-70.
2. J.J. Lewandowski, C. Liu, and W.H. Hunt: *Mater. Sci. Eng.*, 1989, vol. A107, pp. 241-55.
3. S.V. Kamat, J.P. Hirth, and R. Mehrabian: *Acta Metall.*, 1989, vol. 37, pp. 2395-2402.
4. Y. Flom and R.J. Arsenault: *Acta Metall.*, 1989, vol. 37, pp. 2413-23.
5. M. Manoharan and J.J. Lewandowski: *Scripta Metall. Mater.*, 1990, vol. 24, pp. 2357-62.
6. M. Manoharan and J.J. Lewandowski: *Acta Metall. Mater.*, 1990, vol. 38, pp. 489-96.
7. T.F. Klimowicz and K.S. Vecchio: in *Fundamental Properties of Metal-Matrix Composites*, P.K. Liaw and M.N. Gungor, eds., TMS-AIME, Warrendale, PA, 1990, pp. 255-67.
8. A. Mortensen: in *Fabrication of Particulates Reinforced Metal Matrix Composites* ASM, Materials Park, OH, 1990, p. 217.
9. D.J. Lloyd: *Acta Metall. Mater.*, 1991, vol. 39, pp. 59-71.
10. J.J. Lewandowski, D.S. Liu, and C. Liu: *Scripta Metall.*, 1991, vol. 25, pp. 21-26.
11. Z. Wang, T.K. Chen, and D.J. Lloyd: *Metall. Trans. A*, 1993, vol. 24A, pp. 197-207.
12. W.H. Hunt, T.M. Osman, and J.J. Lewandowski: *J. Met.*, 1993, Jan. pp. 30-35.
13. I. Dutta, C.F. Tiedemann, and T.R. McNelley: *Scripta Metall. Mater.*, 1990, vol. 24, pp. 1233-38.
14. J. Llorca, A. Needleman, and S. Suresh: *Acta Metall. Mater.*, 1991, vol. 39, pp. 2317-35.
15. Y.L. Shen, M. Finot, A. Needleman, and S. Suresh: *Acta Metall. Mater.*, 1994, vol. 42, pp. 77-97.
16. I. Dutta, J.D. Sims, and D.L. Seigenthaler: *Acta Metall. Mater.*, 1993, vol. 41, pp. 885-908.
17. A. Levy and J.M. Papazian: *Acta Metall.*, 1991, vol. 39, pp. 2255-66.
18. T.R. McNelley and P.N. Kalu: *Scripta Metall. Mater.*, 1991, vol. 25, pp. 1041-46.
19. R. Kapoor and K.S. Vecchio: *Mater. Sci. Eng.*, 1995, vol. A200, pp. 63-75.
20. I. Dutta and B.S. Majumdar: *Mater. Forum*, 1996, vols. 217–222, pp. 1473-78.
21. J.C. Lee and K.N. Subramanian: *J. Mater. Sci.*, 1993, vol. 28, pp. 1578-84.
22. W.H. Hunt, J.R. Brockenbrough, and P.E. Magnusen: *Scripta Metall. Mater.*, 1991, vol. 25, pp. 15-20.
23. F.W. Longenecker: Master's Thesis, Naval Postgraduate School, Monterey, CA, 1993.

24. F.R. Stonesifer and R.W. Armstrong: in *Advances in Research on the Strength and Fracture of Materials*, vol. 2A, *Physical Metallurgy of Fracture*, C.M.R. Taplin, ed., 1977, Pergamon, Oxford, United Kingdom, p. 1.
25. D.A. Curry and J.F. Knott: *Met. Sci.*, 1976, vol. 10, p. 1.
26. R.W. Armstrong: *Can. Met. Q.*, 1974, vol. 3, p. 187.
27. R.W. Armstrong: *Trans. Ind. Inst. Met.*, 1986, vol. 39, p. 85.
28. W.L. Li and J.C.M. Li:*Phil. Mag.*, 1989, vol. 59, pp. 1245-61.
29. F.J. Humphreys: *Acta Metall.*, 1977, vol. 25, pp. 1323-44.
30. F.J. Humphreys, W.S. Miller, and M.R. Djazeb: *Mater. Sci. Technol.*, 1990, vol. 6, pp. 1157-66.
31. W.S. Miller and F.J. Humphreys: *Scripta Metall.*, 1991, vol. 25, p. 35.
32. P.N. Kalu and T.R. McNelley: *Scripta Metall.*, 1991, vol. 25, p. 853.
33. F.J. Humphreys and P.N. Kalu: *Acta Metall.*, 1990, vol. 38, p. 917.
34. F.J. Humphreys and P.N. Kalu: *Acta Metall.*, 1987, vol. 35, pp. 2815-29.
35. *Product Technical Literature*, DWA Composite Specialties, Chatsworth, CA.
36. I. Dutta, C.P. Harper, and G. Dutta: *Metall. Mater. Trans. A*, 1994, vol. 25A, pp. 1591-1602.
37. M.R. van den Bergh: *DWA Composite Specialties*, Chatsworth, CA, personal communications, 1997.
38. G. Thomas: *Transmission Electron Microscopy of Metals*, John Wiley & Sons, New York, NY, 1964.
39. I. Dutta and S.M. Allen: *J. Mater. Sci. Lett.*, 1991, vol. 10, pp. 323-26.
40. I. Dutta, S.M. Allen, and J.L. Hafley: *Metall. Trans. A*, 1991, vol. 22A, pp. 2553-63.
41. N.J. Petch: *J. Iron Steel Inst.*, 1953, vol. 174, p. 25.
42. N.J. Petch: *Progr. Met. Phys.*, 1954, vol. 5, p. 1.
43. J. Heslop and N.J. Petch: Petch: *Phil. Mag.*, 1958, vol. 3, p. 1128.
44. B.A. Bilby, A.H. Cottrell, and K.H. Swinden: *Proc. R. Soc. A*, 1963, vol. 272, pp. 304-14.
45. J. Pacyna and M. Mazur: *Scand. J. Met.*, 1983, vol. 12, p. 22.
46. M. Vogelsang, R.J. Arsenault, and R.M. Fisher: *Metall. Trans. A*, 1986, vol. 17A, pp. 379-89.
47. *Metals Handbook*, vol. 12, *Fractography*, 9th ed., ASM INTERNATIONAL, Metals Park, OH, 1987, p. 20.
48. H. Mecking and U.F. Kocks: *Acta Metall.*, 1991, vol. 29, pp. 1865-75.